International Journal of Thermodynamics (IJoT)
ISSN 1301-9724 / e-ISSN 2146-1511
https://dergipark.org.tr/en/pub/ijot

Vol. 25 (No. 4), pp. 24-34, 2022
doi: 10.5541/ijot.1129559
Published online: December 1, 2022

Research Article

Emissivity Prediction for an IR Camera During Laser Welding of Aluminum

*A. Metallo

Industrial Engineering Department, University of Salerno, Italy
E-mail: antonio.metallo@libero.it

Received 12 June 2022 Revised 6 September 2022, Accepted 25 October 2022

Abstract

Laser processing is becoming increasingly important in industrial applications. The success of the process relies on two fundamental parameters: the surface temperature of the medium and the thickness of the hardened layer. One of the most important factors during a laser process is certainly the temperature, which presents high temperature gradients. The speed at which a material undergoes a phase transition, the chemical reactions that take place during processing and the properties of the material are all dependent on temperature changes. Consequently, the measure of temperature is a demanding undertaking. This study proposes to measure temperature for the duration of laser welding with the infrared camera (IR) Optris PI. To restore the real temperature based on the brightness temperature values measured by the IR camera is needed to evaluate the emissivity to be attributed to the IR camera. For this purpose, firstly, the isotherms consistent with the melting point of aluminum (785 K) were assessed and then compared with the temperature distribution gauged in the zone of irradiation of the laser. Such data were then compared with the thickness of the melted zone. The use of the melting point isotherm allowed the calculation of the value of emissivity and the restoration of the temperature. Thermography software data acquisition wrongly presupposes the emissivity value does not change. This generates incorrect thermographic data. The surface emissivity normally hinges on temperature. Therefore, the values on which the literature relies may not work for materials of interest in the conditions of the process. This is particularly the case, where welding is carried out in keyhole mode ($T_{max} = T_{vap}$). However, the physical phenomena involved, including evaporation and plasma plume formation, high spatial and temporal temperature gradients, and non-equilibrium phase transformations, influence the optical conditions of the brightness of the emission of light from the molten pool, making, De Facto, the emissivity value not constant. Thus, what we propose here is a methodological procedure that allows the measurement of the effective emissivity of the surface, at the same time taking into consideration the consequence of physical phenomena and the conditions of the surface. Two procedures (Standard and Simplified) capable of providing the correct emissivity value in relation to the working parameters have been proposed. The results showed that the procedures are correct, fast, and easy to use.

Keywords: *Laser welding; emissivity; thermography; IR camera calibration.*

1. Introduction

Typically, the temperature of the object is one of the fundamental parameters of thermal processes [1,3,10], such as example, melting. As a consequence, it must be evaluated accurately. But this is not an easy task for several reasons. Primarily under laser processing, the temperatures reach high values with high-temperature gradients. A few metrological points are evident here. These include: a range of temperature that goes up to 2000 K and remarkable temperature gradients (~ 105 –107 K/m) both in the pool where melting is performed and the zone affected by heat; elevated rates of heating and cooling (~ 103 –106 K/s); flexible laser beam diameter in the plane of focus (ranging from 50 μm to 500 μm), a reflection of the laser beam, phenomena of the plume where the laser works, and emissivity of temperature dependence [4]. Compare to photoelectric detectors, thermal detectors such as thermocouples or semiconduction bolometers, which are much more susceptible to change in temperature on the sensor, possess a lower sensitivity and their reaction time is much slower. Photoelectric detectors can instead register infinitesimal changes in the flow of thermal radiation. In this case, only a minimal part of the full flow of the heat released by the surface of a heated body could be recorded. Laser metalworking temperature measurements are typically executed with thermocouples, infrared cameras, and pyrometers [7]. In any case, the need to obtain temperature data that are extremely precise and with a high resolution in space and time is a remarkable task for experimenters, where temperatures, gradients, and rates of heating and cooling are severely extreme [8]. There are other crucial problems for the infrared camera in such an environment. The problem here is that the emissivity of the hot metal is both low and inconsistent in this environment, where the temperatures are deducted, and therefore apparent (or better relative), and thus not true (or better absolute). Infrared (IR) thermography is the use of an IR camera to measure the apparent temperature of an object derived from its emissivity [9]. Therefore, the measurement of temperature through infrared radiation necessitates knowing the value of the emissivity of the heated surface both in the whole spectrum of range

*Corresponding Author

sensitivity and in the full space of the temperature used in the process. The surface emissivity usually depends on the:

- Material
- Surface quality (geometry, roughness, oxidation, etc.)
- IR Camera (wavelength and the direction of observation)
- Temperature
- physical phenomena : phase change, evaporation, plasma plume formation, etc.

Most of the existing literature, that employs thermography in the evaluation of the welding process, is grounded on unchanging values of emissivity. This is the consequence of insufficient knowledge of the modification of the emissivity in the material through the process of welding. Examples of this literature, that gauge thermal signature in the processes of welding through a method of thermography grounded in an unchanging value of emissivity, are Boillot et al., Chen and Feng and Woo et al. Others [11,12,13] have evaluated the emissivity as a function of temperature, not going beyond the melting temperature, thus neglecting the effects due to the phase change. Thus, most of the available data did not consider the effects of the physical phenomena on the emissivity value. For this purpose, some authors [3,7] have proposed an alternative method for the evaluation of emissivity during laser welding. The isotherms consistent with the melting point of aluminum (785 K) were assessed and then compared with the temperature distribution gauged in the zone of irradiation of the laser. Such data were then compared with the thickness of the melted zone. The use of the melting point isotherm allowed the calculation of the value of emissivity and the restoration of the temperature [4]. In this way, the emissivity is evaluated by considering the effects due to phase change and evaporation. However, the authors hypothesize that the value obtained is constant. The physical phenomena involved, including evaporation and plasma plume formation and in general, all those physical phenomena that influence the emissivity, mostly depend on the working parameters chosen as they determine the energy supplied during laser processing which in turn determines the temperature gradient. The temperature gradient determines the speed of phase transitions, evaporation rate, chemical reactions, microstructure and properties of the material, [2-3]. As is evident, that whenever the parameter values change, supply energy and the width of the melted zone change, and consequently the emissivity value changes [3,6]. This requires the need to carry out preliminary tests. The purpose of this work is to create a methodology that allows one to obtain an emissivity as a function of a w_{mz} and evaluate it without carrying out tests on the laser machine.

Once the material for a process by laser is chosen, the tests are made with the identical quality of the surface, and the IR camera is selected and placed, the emissivity will be the outcome of temperature and other associated physical phenomena. Furthermore, if the welding takes place in key-hole mode, and then in conditions where the maximum temperature reached is always the same ($T_{max} = T_{vap}$), the functional dependence of the emissivity can be reduced exclusively to the development of the physical phenomena involved. The evolution of the physical phenomena described largely depends on the working parameters (P - laser supplied power, v - welding speed, d - defocus), consequently, the emissivity was evaluated as a function of these $\varepsilon = f(d, P, v)$. It has also been noted that if the defocus value is fixed, the width of the melted zone depends on the working parameters P and v, thus obtaining the relation: $w_{mz}=f_d(P,v)$. In this way, it was possible to obtain a relationship between the emissivity (ε) and the width of the melted zone (w_{mz}) for a fixed defocus value.

$$\varepsilon_0 = f_0(w_{mz}) \quad (1)$$

$$\varepsilon_{-6} = f_{-6}(w_{mz}) \quad (2)$$

With this methodology it is possible to evaluate the emissivity as a function of width of the melted zone. The emissivity was then obtained by carrying out two types of tests by setting the defocus to two different values (d_0, d_{-6}) and varying the other two parameters P and v. After the tests, the experimental sets of (w_{mz}, ε) were fitted by the empirical model. Through interpolating procedure, the functions relating to the other defocus values have been obtained. The emissivity map (Figure 1), which establishes the relationship between the emissivity and the width of the melted zone is then obtained. Then, a FEM model, using COMSOL Multiphysics software, was created. The FEM model was validated by comparing the isotherm corresponding to the melting point ρ_y to the width of the melted zone (w_{mz}) derived from experimental tests.

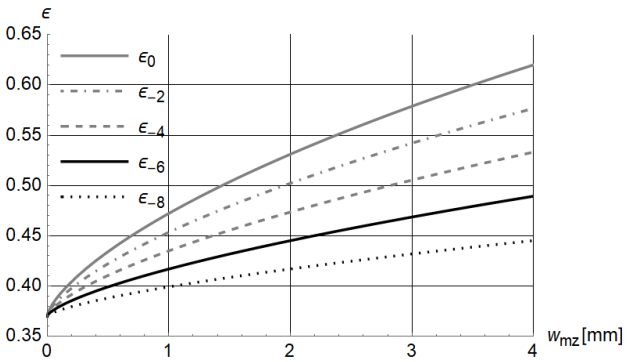

Figure 1. The emissivity map.

So, it is possible to evaluate the emissivity for different working parameters by first evaluating the isotherm corresponding to the melting point ρ_y, obtained through the FEM model. (Standard procedure).

To reduce times, and to obtain a faster and more practical procedure, the parameter map was obtained. The knowledge of the parameter map allowed a relationship between specific energy and the width of the melted zone, corresponding to a preselected value for the defocus. It was able to value the width of the melted zone $w_{mz} = w_{mz,i}(e_{LB})$ after fixed parameters and calculated the specific energy. From the emissivity map, the emissivity value is then obtained. (Simplified procedure).

2. Materials and Method

It was considered a base metal corresponding to the standard EN 45100 (AlSi5Cu3Mg – UNI EN 1676) aluminum with a thickness of 6 mm (Table 1). The rectangular section plates have been obtained from a single slab with surface roughness Ra = 1.4 μm.

Table 1. Nominal Chemical Composition (wt %) of Base Metals.

chemical components	%
Si	4.5÷6
Fe	0.5
Cu	2.6÷*3.6*
Mn	0.55
Mg	0.20÷*0.45*
Cr	/
Ni	0.1
Zn	0.1
Sn	0.05
Ti	0.2

For the purposes of this work, a Yb: YAG disk laser source supplied in fiber, operating in continuous wave emission, was considered (Table 2).

Table 2. Laser Welding System Technical Data.

Chemical Components	%
Maximum output power [kW]	4.0
Laser light wavelength λ [nm]	1030
Beam Parameter Product [nm x mrad]	8.0
Focal beam waist d [mm]	0.3
Rayleigh range [mm]	2.81
Focal length f [mm]	200
Maximum power density [kW/mm^2]	56.6
Laser beam diameter at defocus 0 [mm]	0.3
Laser beam diameter at defocus -2 [mm]	0.44
Laser beam diameter at defocus -4 [mm]	0.71
Laser beam diameter at defocus -6 [mm]	1.01
Laser beam diameter at defocus -8 [mm]	1.32

An integrated 3-way power nozzle was attached to the laser head, which was moved by a 6-axis industrial robot with a dedicated controller. Argon was injected as a carrier gas at a flow rate of 30 L/min, and helium was coaxially blown to the laser beam at a flow rate of 10 L/min as a shielding gas on the melting bath (Figure 2).

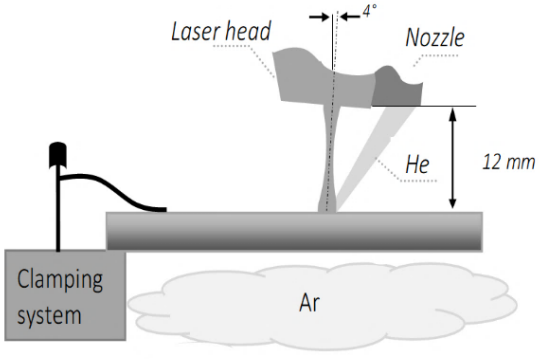

Figure 2. Schematic of the laser head with three-way feed nozzle; components not to scale.

A tilt angle of 4◦ was set for the laser head, in accordance with common practice for processing highly reflective metals [8] to prevent rear reflections from entering the optical train. The infrared (IR) camera (Optris PI 400, spectral wavelength λ=8 μm) was positioned at 0.5 m with a zenith angle of 90° and an azimuth angle of 90°, with respect to the work area, to detect the surface temperature range. An inclination of 45° has been assigned to the IR camera [9]. Therefore, the thermo-chamber mainly acquires emissions from the weld seam visible through the vapor plume. (Figure 3).

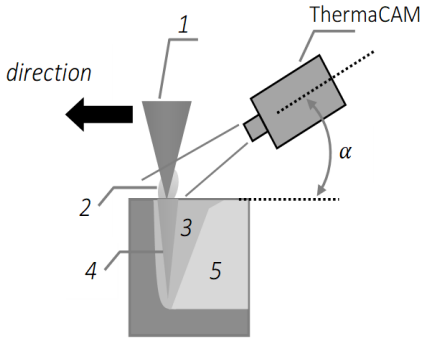

Figure 3. Configuration used for observation with a Optris PI 400 thermal camera. keyhole mode laser welding (1. laser beam, 2. plasma/vapor cloud, 3. molten metal. 4. keyhole. 5. solidified melt).

The calibration of the IR camera was performed by an M390S black body. Emissivity values are defined by Planck's law [24]

$$\frac{1}{T_v} = \frac{1}{T_b} + \frac{\lambda}{c_2} Log(\varepsilon) \tag{3}$$

with T_v - real temperature (K), T_b – brightness temperature (K), c_2 - constant = 14390 (μm K). To measure the geometric characteristics of laser welding, in particular the dimensions of the weld bead, it was using an optical microscope. The experimental sets of (w_{mz}, ε) were fitted, for a fixed defocus value, by the empirical model:

$$\varepsilon_{def,i}(w_{mz}) = 0.37 + Log\left(\frac{x^{0.7}}{C_{def,i}} + 1\right) \tag{4}$$

where $C_{def,i}$ are the best fit parameters (Table 3).

Table 3. Best Fit Parameters.

Emissivity Map		*Parameter Map*	
$C_{def,0}$	19.307	$C'_{def,0}$	11.107
$C_{def,-2}$	10.586	$C'_{def,-2}$	3.915
$C_{def,-4}$	13.755	$C'_{def,-4}$	1.477
$C_{def,-6}$	8.540	$C'_{def,-6}$	0.572
$C_{def,-8}$	31.534	$C'_{def,-8}$	0.285

For each test the specific energy supplied is evaluated as shown:

$$e_{LB} = \frac{P}{A} \cdot \frac{s}{v} \tag{5}$$

where P is a laser supplied power, v is a welding speed, s is the length of the weld (10 cm for all tests) and $A=\pi\cdot(d/2)^2$ is a beam spot area. The experimental sets of (e_{LB}, w_{mz}) were fitted, for a fixed defocus value, by the empirical model:

$$w_{mz,i}(e_{LB}) = Log\left(\frac{x^{1.1}}{C'_{def,i}} + 1\right) \tag{6}$$

where $C'_{def,i}$ are the best fit parameters (Table 3).

3. Mathematical Formulation

For heat transfer and fluid flow modeling, conservation of energy Eq. (7) and mass Eq. (14), and momentum balance Eq. (13) are solved. The following assumptions are made in the model.

- Liquid metal is incompressible Newtonian under flow
- Gaussian heat source
- Boussinesq approximation is valid

$$\rho \cdot c_p^{eq} \frac{\partial T}{\partial t} + \rho \cdot c_p^{eq} u \cdot \nabla T = \nabla \cdot (k \nabla T) \quad (7)$$

with ρ - local density (kg·m^{-3}), c_p^{eq}– local equivalent heat capacity (J·kg^{-1}K^{-1})), k – local thermal conductivity (W·m^{-1}K^{-1}), T – solved temperature (K) and t – time (s). Latent heat of fusion and evaporation are taken in account by means of equivalent enthalpy approach [14].

$$c_p^{eq} = c_p + D_m L_m + D_v L_v \quad (8)$$

where c_p is heat capacity as function of temperature, L_m and L_v – latent heat of fusion and evaporation, and D_m and D_v are Gauss function normalized around melting and evaporation temperature T_m and T_v respectively:

$$D_i = \frac{e^{-\left(\frac{T-T_i}{\Delta T}\right)^2}}{\sqrt{\pi}\Delta T} \quad (9)$$

where ΔT is smoothing interval of 50 K. The initial condition is given by Eq. (10),

$$T(x, y, z, t) = T_0 \quad (10)$$

where the initial temperature T_0 is maintained at 293 K. The convective cooling and surface to ambient radiation boundary conditions were applied to the whole geometry. A heat source was introduced as a top surface Gaussian thermal source. Heat loss due to evaporation was modeled using a top surface vaporization heat flux [15]:

$$\dot{q}_{vap} = -\beta_r L_v \sqrt{\frac{M}{2\pi RT}} P_{sat} \quad (11)$$

where β_r– the specific energy coefficient, L_v – local latent heat of vaporization (J·kg^{-1}), M – molar mass (kg·mol^{-1}), R – ideal gas constant (J·mol^{-1} K^{-1}), P_{sat} – saturated vapor pressure (Pa). The boundary conditions, heat flux and heat of vaporization, applied on the top, is expressed in Eq. (12)

$$k \frac{\partial T}{\partial z}\Big|_{z=6} = -\dot{q}_{gauss} + \square \cdot (T(x, y, 0, t) - T_\infty) + \varepsilon \cdot \sigma \cdot (T^4(x, y, 0, t) - T_\infty^4) + \dot{q}_{vap} \quad (12)$$

where $\dot{q}_{gauss}$ is the specific energy of the beam with a power P with a Gaussian function.

The heat transfer model was incorporated with the fluid flow Multiphysics to determine the deformation of the molten weld pool under various boundary conditions such as Marangoni convection, Buoyancy Darcy damping force and recoil pressure to predict the weld bead morphology. The equations of mass conservation Eq. (13) and momentum balance (Navier-Stokes, Eq. (14)) were used to govern the fluid flow in weld.

$$(\nabla \cdot u) = 0 \quad (13)$$

$$\rho \frac{\partial u}{\partial t} + \rho(u \cdot \nabla)u = \nabla \cdot \left(-pI + \mu(\nabla u + (\nabla u)^T)\right) - \rho\left(1 - \beta(T - T_m)\right)g + F_D \quad (14)$$

where, F_D is the Darcy force (N),

$$F_D = \rho \cdot g \cdot \alpha(T - T_m) \quad (15)$$

g is the acceleration due gravity, α is the coefficient of thermal expansion (K^{-1}) and T_m is the melting temperature. It is found through Rayleigh's analysis that buoyancy force can make a big difference to the temperature profile of the pool via natural convection only when Rayleigh number exceeds 1100 in the pool. In a typical laser welding process, it is far less than 1100 due to small thickness of workpiece and thermal expansion coefficient [16]. Marangoni convection is a fluid flow due to the surface tension in the molten weld pool. It's assigned to the boundary on the top surface

$$-\mu \frac{\partial \mu}{\partial x} = \frac{\partial T}{\partial y} \cdot \frac{\partial \gamma}{\partial T} \quad (16)$$

where μ is the dynamic viscosity (Pa·s) and γ is the temperature derivative of surface tension. At the top surface of the domain, the recoil pressure [17] was applied:

$$P_r = \left(\frac{1+0.02}{2}\right) P_{sat} \quad (17)$$

with pressure of saturated vapor given as:

$$P_{sat} = P_0 \cdot exp\left(\frac{L_{vap} \cdot M}{R}\left(\frac{1}{T_{vap}} - \frac{1}{T}\right)\right) \quad (18)$$

3.1 Numerical Modeling: Finite Element Method

The FEM model was built using COMSOL Multiphysics software. The model is created using heat transfer in fluids and laminar flow under phase change conditions. Multiphysics coupling is achieved by interrelating the equations that describe heat transfer and flow: the velocity field in the equation describing convection (heat flow) is obtained by solving the Navier-Stokes equations, which provide temperature as a function of position; in turn, temperature defines thermophysical properties. To build FEM model correctly, the following have been defined:

Model parameters: needed to build the numerical model such as the type of materials, sample size, wavelength, and work parameters: power, scan speed and spot radius (Table 2).

Materials' Properties: Since the proposed model considers the solid-liquid phase change, the properties at ambient temperature for the solid phase and at melting temperature for the liquid phase were used. Specific heat, thermal conductivity coefficient [18,22], and density [11,19] were then defined (Table 4). The absorption value was chosen for aluminum 0.16 [20,21]. The liquid-vapor phase transition was not considered.

Geometry and mesh modeling: One of the most important steps in FEM modeling is the definition of mesh geometry. The geometry of the model consists of a thin sheet. A 3-D solid block of (40 x 30 x 6) mm^3 was created. To verify that the calculated results are independent of the sample size, some simulations were carried out with the real dimensions of the specimen, and it was verified that the temperature profiles are identical. To ensure that the calculated results are grid-independent, several grid distributions have been tested.

Maximum temperature differences of the fields are less than 0.1 percent by doubling the mesh nodes. Two parts are meshed using tetrahedral geometry meshes. The minimum and maximum size of the element for the mesh is 0.1 and 0.2 mm for the block where one boundary condition has been applied and 0.2 and 0.3 mm for the other.

Table 4. Aluminum Thermophysical Properties.

	Phase State	
	Solid	Liquid
ρ [kg m^{-3}]	2600	2400
k [W m^{-1} K^{-1}]	150	90
μ [Pa s]	0.001	0.0007
L_m [J kg^{-1}]	$3.3 \cdot 10^5$	
L_v [J kg^{-1}]	$1.4 \cdot 10^7$	
c_p [J kg^{-1} K^{-1}]	Eq. (8)	
σ [N m^{-1}]	0.7	
T_m [K]	785	
T_{vap} [K]	2800	
M [kg mol^{-1}]	0.269	
R [J·mol^{-1} K^{-1}]	8.314	

Boundary conditions and initial conditions: The laser beam incident on the surface z = 6 mm was characterized by a second type boundary condition where the imposed flux is the heat source $\dot{q}_{gauss}$. In addition, the third type boundary condition on face z = 6 mm was considered. In the hypothesis of natural convection $\dot{q}_{conv}$, the model was given a constant thermal convection coefficient h = 10 [W m^{-2} K^{-1}] [21,23]. It was also considering radiative cooling $\dot{q}_{irr}$ a constant value was set $\varepsilon_{irr} = 0.15$ [12] for aluminum. Furthermore, the third type of boundary convective condition on all faces was considered (Figure 4).

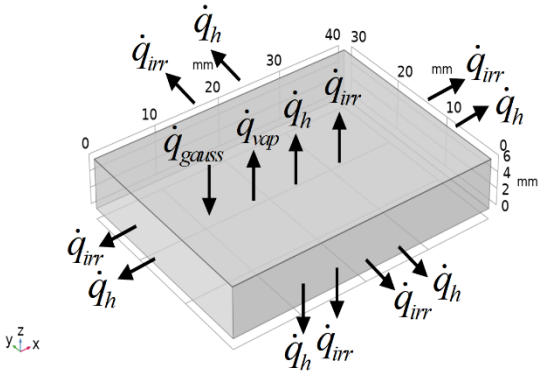

Figure 4. The schematization of the boundary conditions.

The ambient temperature and the initial temperature conditions of the plate are equal to 293 K. The liquid-vapor phase transition was not considered. On the other hand, the heat loss through evaporation was represented by top surface vaporization heat flux $\dot{q}_{vap}$ Eq. (11). The specific energy coefficient was introduced to consider the specific energy supplied during laser welding. The coefficients have been obtained considering that the specific energy supplied during laser welding depends mainly on the diameter of the laser beam. In particular, the specific energy increases as the diameter decreases. Since β_r and the supplied energy coefficients are directly proportional, because if the specific energy supplied increases, the energy lost by evaporation must increase, β_r and the diameter are inversely proportional (Table 5) At the top surface of the domain, the recoil pressure was applied P_r Eq. (17). Finally, Marangoni effect was considered the surface tension coefficient (σ) at the melting temperature T_m was taken into consideration [19].

Table 5. The Specific Energy Coefficient.

Defocus	Diameter d [mm]	1/d	βr - min normalization
def_0	0.3	3.33	4.4
def_{-2}	0.44	2.27	3
def_{-4}	0.71	1.41	1.9
def_{-6}	1.01	0.99	1.3
def_{-8}	1.32	0.76	1

Laser beam modeling: We assume that in the z-direction the heat source is concentrated at a level immediately below the upper surface (z = 6 mm). The irradiation of the beam gradually decreases at the edges (Figure 5).

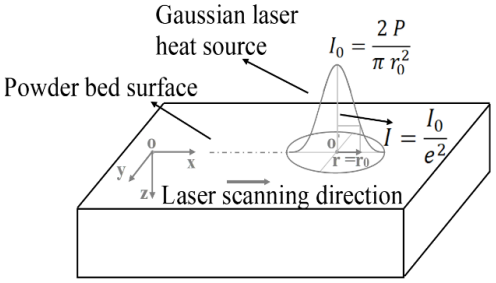

Figure 5. Sketch of the workpiece and coordinate system.

To define beam width for Gaussian beams Eq. (19) was used a $1/e^2$ method.

$$\dot{q}_{gauss}(x,y) = \frac{2 \cdot P}{\pi \cdot {r_0}^2} Exp\left(-\frac{2 \cdot ((x-x_0)^2+(y-y_0)^2)}{{r_0}^2}\right) \quad (19)$$

The width of the beam is calculated by measuring the distance between the two points where the intensity is $1/e^2$ of the peak value (Figure 6). So only about 86.5 % of the laser power is contained within the $1/e^2$ width (Eq. (20), Table 6).

$$\int_{x=-\sigma}^{\sigma} \int_{y=-\sigma}^{\sigma} \dot{q}_{gauss}(x,y) \cdot dxdy = 86.5\%P \quad (20)$$

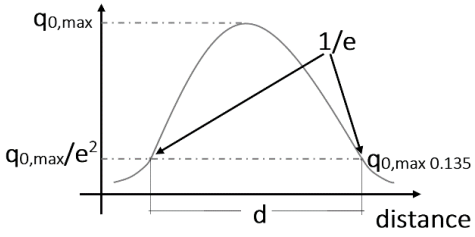

Figure 6. Gauss laser beam modelling.

4. Result and Discussion

4.1 Experimental Tests

Two types of tests were carried out at different defocus values as shown in Table 6. A rectangular section plate of sizes (L_x=100 x L_y=50 x L_z=6 mm) was used.

Each test was analyzed under an electron microscope which made it possible to obtain an image of the trace in TIF format (Figure 7).

The traces were divided into 17 sections at 4 mm intervals. For each section the size of the trace was evaluated (Table 7).

Table 6. Welding System Technical Data.

	Power P[W]	Welding speed v [mm s^{-1}]	Defocus def [mm]	Beam Diameter d [mm]
1AL	2500	50	0	0.30
2AL	3000	50	0	0.30
3AL	3000	35	0	0.30
5AL	3500	50	-6	1.01
8AL	3750	40	-6	1.01
9AL	4000	40	-6	1.01

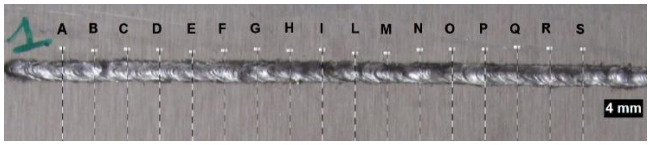

Figure 7. Electronic microscope image: Test 1AL weld track.

Table 7. Test 1AL Width of the Melted Zone Sections.

Sez.	s[mm]	Sez.	s[mm]
a	2.26	m	2.57
b	2.34	n	2.49
c	2.34	o	2.44
d	2.16	p	2.57
e	2.34	q	2.39
f	2.55	r	2.39
g	2.34	s	2.39
h	2.49	Mean	2.40
i	2.34	Dev.St	0.11
l	2.31		

Then, mean values and standard deviations are calculated (Table 8).

Table 8. Mean Value of a Width of the Melted Zone.

Test	Width of the melted zone w_{mz}[mm]	Dev. st
1Al	2.40	0.11
2Al	2.58	0.15
3Al	2.88	0.15
5Al	2.87	0.10
8Al	3.18	0.13
9Al	3.40	0.08

These results will be used to validate the numerical model. For this purpose, the isotherms corresponding to the melting point (ρ_y) were calculated through the finite element method. The calculated ρ_y data were compared with the width of the melted zone (w_{mz}).

4.2 FEM Results

The simulation process allowed us to extrapolate the values corresponding to the fusion isotherm (785 K) on the plane at z =6 mm.

The data were fitted using an ellipsoidal model, Eq. (21)

$$\begin{cases} x(r) = X_0 + a \cdot \cos\theta_r \\ y(r) = Y_0 + b \cdot \sin\theta_r \\ 0 \le \theta_r \le 2 \cdot \pi \end{cases} \quad (21)$$

with a - sub axis (radius) of the X axis of the non-tilt ellipse, b - sub axis (radius) of the Y axis of the non-tilt ellipse, X_0 - center at the X axis of the non-tilt ellipse, Y_0 center at the Y axis of the non-tilt ellipse, ρ_x - size of the long axis of the ellipse, ρ_y - size of the short axis of the ellipse, φ - orientation in radians of the ellipse (tilt). In this way, it was possible to quickly obtain the value of the diameter corresponding to the melting point (ρ_y) (Table 9, Figure 9).

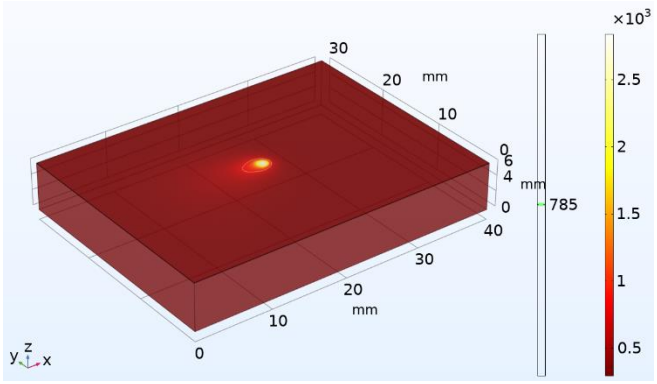

Figure 8. FEM Test 1AL, ρ_y isotherm at T=785K.

Table 9. FEM Fit Parameter.

	1AL.	2AL	3AL	5AL	8AL	9AL	4AL	6AL
a	1.772	1.874	1.924	2.473	2.485	2.513	1.897	2.286
b	1.236	1.287	1.350	1.532	1.649	1.659	1.293	1.458
φ	-0.006	-0.007	0.025	-0.010	0.005	0.003	-0.008	-0.016
X_0	19.310	19.253	15.79	19.006	16.813	16.83	19.29	19.19
Y_0	14.855	14.845	15.387	14.779	15.074	15.03	14.81	14.67
ρ_x	3.544	3.748	3.849	4.946	4.971	5.026	3.795	4.573
ρ_y	2.473	2.574	2.719	3.045	3.299	3.318	2.586	2.917
Err %	0.225	0.26	0.268	0.402	0.684	0.109	0.211	0.107

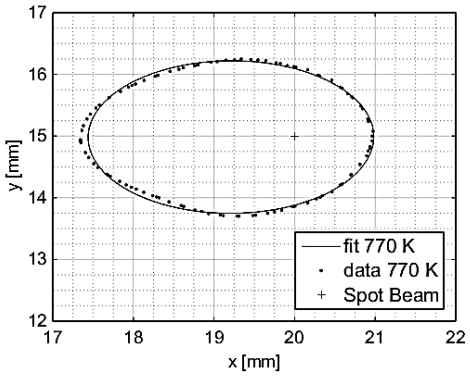

Figure 9. 1AL numerical data fit time = 0.2 s

As shown in Table 10,

Table 10. Isotherm Corresponding to the Melting Point Compared with the Width of the Melted Zone.

	P[W]	v [mm s^{-1}]	def [mm]	w_{mz}	ρ_y	err %
1AL	2500	50	0	2.40	2.477	3.02
2AL	3000	50	0	2.58	2.575	0.20
3AL	3000	35	0	2.88	2.720	5.75
5AL	3500	50	-6	2.87	3.045	5.92
8AL	3750	40	-6	3.18	3.299	3.67
9AL	4000	40	-6	3.40	3.318	2.44
4AL	3000	50	-4	2.60	2.586	0.50
6AL	2500	50	-8	2.87	2.917	1.63

fixed beam diameter and scan speed, as the power delivered by the laser increases, the extension of the diameter corresponding to the melting temperature increase (Tests 1AL and 2AL). The diameter ρ_y also increases with decreasing speed. For each test, the percentage error

between the isotherms corresponding to the melting point (ρ_y numerically evaluated) and the extension of the melted zone (w_{mz}, obtained through experimental tests) was evaluated. As shown in Table 10, the error for all types of test results is less than 6%. Thus, the constructed FEM model can provide a useful approximation to reality with a low average error. Then two further tests with defocus values def_{-4} def_{-6} were carried out, to verify the goodness of the FEM model (Table 11).

Table 11. Test Coefficients and Parameters.

P[W]	v[mm·s^{-1}]	def[mm]	d[mm]
3000	50	-4	0.71
3500	50	-8	1.32

It was compared the isotherm corresponding to the melting point to the width of the melted zone (Table 10). Also, in this case, the error is less than 6%.

4.3 Method of Brightness Temperature Definition and Emissivity Evaluation: The Emissivity Map

The thermal image of cladding zone registered by IR camera is presented in Figure 10.

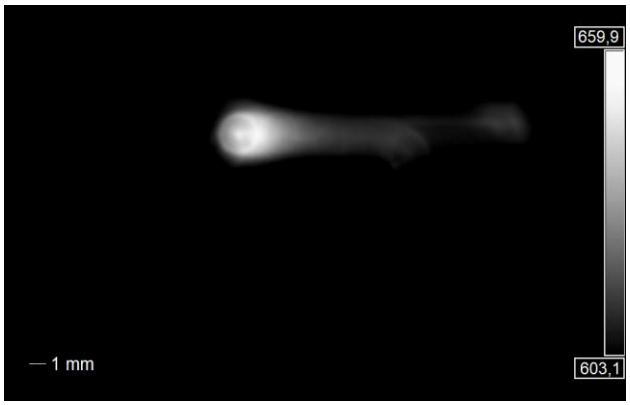

Figure 10. False-color: infrared image of melt pool registered by IR camera optris in 8 μm spectral wavelength, Test 1AL

The laser beam's maximum energy density flux has a pseudo-Gaussian form, which raises the temperature at the beam axis. The periphery portion of the molten pool, where oxides and other nonmetallic inclusions are typically concentrated by thermocapillary convection and in the nearby solid phase sections, correlates to the ring-shaped zone with strong thermal emission. It is possible to define the emissivity value using Planck's law [24] at a spectral value λ=8 μm Eq. (3), assuming that the value of temperature stabilization at solidification corresponds to the known melting point of AL, which is equal to 785 K under equilibrium conditions. The comparison of the width of the molten zone obtained by irradiating the laser beam of the surface aluminum and the IR camera signal value is presented in Table 12.

A different type of palette (integrated in the Optris PI connect program) was used to display the images in such a way as to have well defined the different isotherms (Figure 11).

For each test 8 frames were evaluated (1 every 1 s). The obtained mean value was used to calculate the emissivity Table 13.

Table 12. Mean Brightness Temperature and Emissivity, λ=8 μm.

	w_{mz}[mm]	Brightness temperature Tb [K]	Empirical ε
1AL	2.40	623	0.550
2AL	2.58	635	0.581
3AL	2.88	641	0.597
5AL	2.87	587	0.461
8AL	3.18	596	0.486
9AL	3.40	600	0.493
4AL	2.60	609	0.515
6AL	2.87	577	0.437

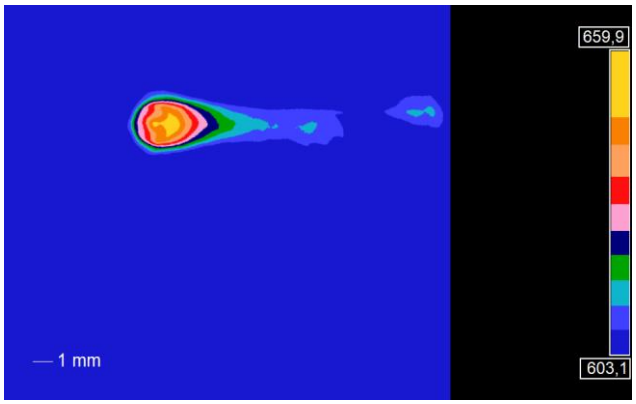

Figure 11. Rainbow-colors: infrared image of melt pool registered by IR camera optris in 8 μm spectral wavelength, Test 1AL frame 4.

Table 13. Brightness Temperature, Frame 1-8.

Frame	1AL	5AL
1	615	579
2	630	577
3	635	594
4	620	597
5	621	598
6	617	579
7	632	581
8	614	590
$\bar{T}$ [K]	623	586.9

The experimental sets of (w_{mz}, ε) were fitted, for a fixed defocus value, by the empirical model, Eq. (4).

Coordinate (0, ε_0) has been identified as a reference. In fact, the condition w_{mz} = 0 represents the case in which the temperature reached is lower than the melting point so that melting does not occur. The value of ε_0 = 0.37 was chosen which corresponds to the emissivity at a temperature of 785 K [25]. The functions relating to the other defocus values have been obtained through interpolating procedure (Table 3, Figure 12).

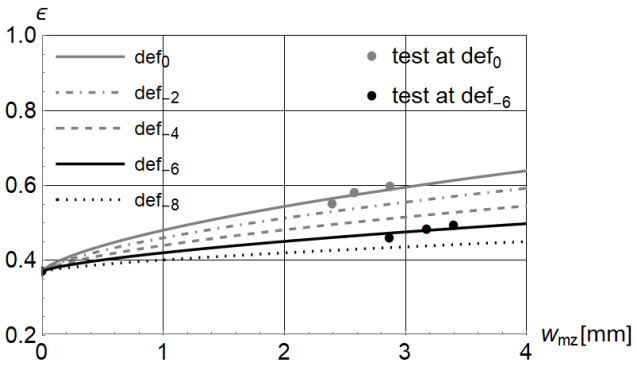

Figure 12. The emissivity map. Functions ε (w_{mz}) at different defocus values.

In this way, the emissivity map, which coupled with the FEM model allows us to obtain a procedure capable of providing the emissivity value without carrying out tests on the laser machine, was obtained. A relative error between the emissivity value evaluated experimentally and that obtained from the emissivity map using experimental w_{mz} was evaluated (Table 14).

Table 14. Experimental Emissivity vs Emissivity Obtained from the Emissivity Map - Input w_{mz} .

	w_{mz} [mm]	Empirical ε	Emissivity map $\varepsilon_{def,i}(w_{mz})$	Err %
1AL	2.40	0.550	0.551	0.2
2AL	2.58	0.581	0.560	3.7
3AL	2.88	0.597	0.574	4.0
5AL	2.87	0.461	0.465	1.0
8AL	3.18	0.486	0.472	2.8
9AL	3.40	0.493	0.478	3.2
4AL	2.60	0.515	0.503	2.3
6AL	2.87	0.437	0.434	0.7

As shown, the error is ≤ 4 %. So, through the parameter map, it is possible to evaluate the correct emissivity value, to be attributed to the IR camera in relation to the working parameters, knowing the width of the melted zone. Since, as previously seen, $w_{mz} = \rho_y$ with less than a maximum error of 6 % to the diameter corresponding to the fusion isotherm, it was possible to use the ρ_y value, obtained from the FEM model as input data for the evaluation of the emissivity with the use of the emissivity map. For 4AL and 6AL tests, respectively to defocus def_{-4} and def_{-8}, the emissivity was evaluated starting from the value of the width of the melting zone w_{mz}, experimentally evaluated, and compared with temperature distribution measured in the laser irradiation zone (Table 14). Also, in this case, a relative error between the experimentally emissivity value and that obtained from the emissivity map using experimental w_{mz} , was evaluated . Then, through the FEM model, the width of the melted zone was evaluated. The emissivity was obtained through the emissivity map ε (ρ_y), (Figure 13, Table 15).

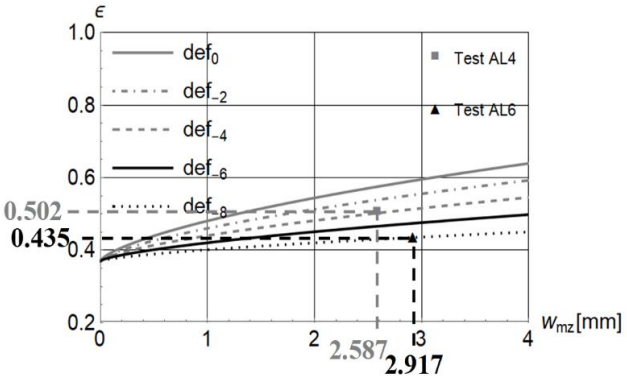

Figure 13. ε (ρ_y) value obtained through the emissivity map. Tests 4AL,6AL.

It has been observed that the use of the methodology involves an error ≤ 5% .

We can sum up, what will be called the standard procedure, as follows (Figure 14):

- *Known the working parameters, through the FEM model the value $w_{mz} = \rho_y$ was obtained.*
- *Using the emissivity map, the value $\varepsilon(\rho_y)$ was obtained.*

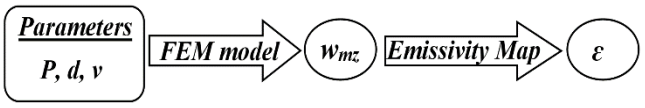

Figure 14. Standard procedure.

Table 15. Experimental Emissivity vs Emissivity Obtained from the Emissivity Map - Input ρ_y - Standard Procedure.

	ρ_y [mm]	Empirical ε	Emissivity map $\varepsilon_{def,i}(\rho_y)$	Err %
1AL	2.477	0.550	0.569	3.5
2AL	2.575	0.581	0.574	1.1
3AL	2.720	0.597	0.582	2.6
5AL	3.045	0.461	0.476	3.4
8AL	3.299	0.486	0.482	0.7
9AL	3.318	0.493	0.484	2.0
4AL	2.587	0.503	0.502	0.1
6AL	2.917	0.434	0.435	0.2

4.4 Method of Specific Energy: The Parameter Map

Through the FEM model, which allows us to evaluate the width of the melting zone for fixed working parameters, and next through the emissivity map, it was possible to obtain the emissivity value to be attributed to the IR camera for correct calibration. In this way, it is possible to predict the emissivity, for fixed working parameters, without having to carry out tests on the laser machine, but simply by obtaining the ρ_y value from the FEM model and then using the emissivity map. Since the computational times are not short (about 4 hours), a streamlined procedure has been implemented. For each test, the specific energy supplied is evaluated (Eq. (5) – Table 16):

Table 16. Specific Energy.

	P [W]	v [mm·s-1]	d [mm]	A [mm²]	e_{LB} [kJ mm⁻²]	w_{mz} [mm]
1AL	2500	50	0.30	0.070	70.735	2.40
2AL	3000	50	0.30	0.070	84.882	2.58
3AL	3000	35	0.30	0.070	121.261	2.88
5AL	3500	50	1.01	0.801	8.730	2.87
8AL	3750	40	1.01	0.801	11.705	3.18
9AL	4000	40	1.01	0.801	9.985	3.40
4AL	3000	50	0.71	0.395	15.154	2.60
6AL	3500	50	1.32	1.369	5.115	2.87

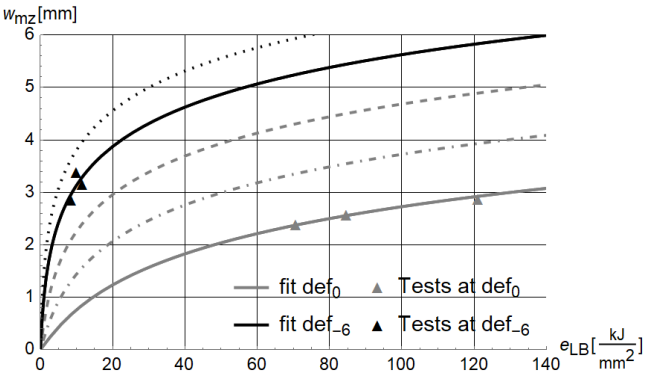

Figure 15. The parameter map. Functions $w_{mz}(eLB)$ at different defocus values.

The experimental sets of (e_{LB}, w_{mz}) were fitted, for a fixed defocus value, by the empirical model, (Table 3, Eq. (6)). In

this case, the point (0,0) corresponding to the condition in which $e_{LB} = 0$ consequently $w_{mz} = 0$, has been identified as a reference. The parameter map (Figure 15), which allows us to predict the width of the melted zone as a function of the working parameters, thus was obtained.

A relative error between the width of the melted zone and $w_{mz,i}(e_{LB})$ obtained from the parameter map, was evaluated (Table 17).

Table 17. Width of the Melted Zone w_{mz} vs $w_{mz,i}(e_{LB})$ Obtained from the Emissivity Map.

	w_{mz} [mm]	e_{LB} [kJ mm^{-2}]	Parameter Map $w_{mz,i}(e_{LB})$ [mm]	w_{mz} Err %
1AL	2.40	70.735	2.37	1.1
2AL	2.58	84.882	2.55	0.9
3AL	2.88	121.261	2.92	1.6
5AL	2.87	8.730	2.99	4.2
8AL	3.18	11.705	3.30	3.7
9AL	3.40	9.985	3.16	7
4AL	2.60	15.154	2.67	2.6
6AL	2.87	5.115	3.02	5.1

The methodology relating to the 4AL and 6AL tests was used. After setting the parameters, the specific energy was evaluated (Table 16).

The $w_{mz,i}(e_{LB})$ was evaluated using the parameter map (Figure 16),

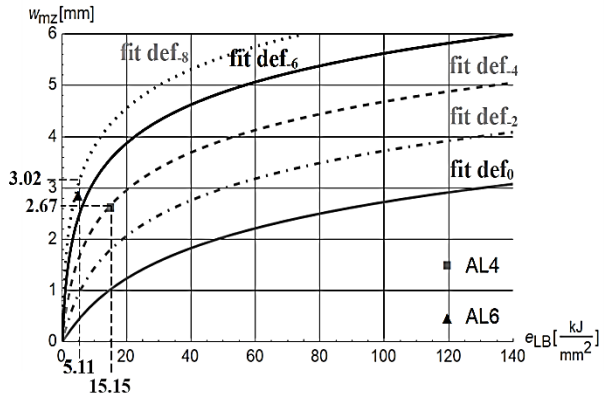

Figure 16. Width of the melted zone obtained through the parameter map. Tests 4AL,6AL.

through the emissivity map (Figure 17) the $\varepsilon(w_{mz,i}(e_{LB}))$ was obtained.

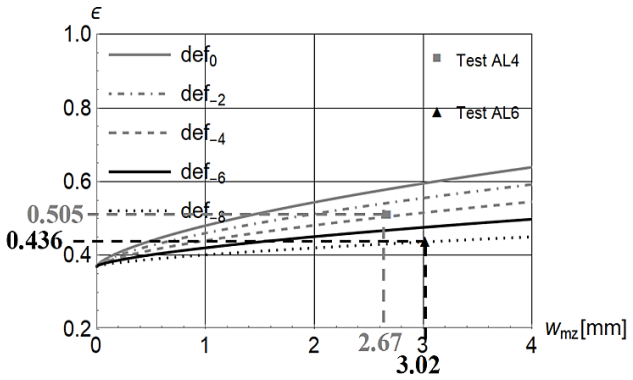

Figure 17. $w_{mz}(e_{LB})$ obtained through the emissivity map. Tests 4AL,6AL.

The results showed that it is possible to approximate the width of the melted zone w_{mz} with the value $w_{mz,i}(e_{LB})$ obtained from the parameter map with an average error equal to 3.3 % and a max error of 7 % (Table 17). The error between the emissivity evaluated empirically and that obtained from the emissivity map using the $w_{mz,i}(e_{LB})$ value obtained from the parameter map is small. The results showed an average error of 1.5 % with a maximum of 3.2 % (Table 18).

Table 18. Empirical Emissivity vs Emissivity Obtained from the Emissivity Map - Input $w_{mz}(e_{LB})$ - Simplified Procedure.

	Parameter Map $w_{mz,i}(e_{LB})$ [mm]	Emissivity Map $\varepsilon(w_{mz}(e_{LB}))$ [mm]	Empirical ε	ε Err %
1AL	2.37	0.564	0.550	2.6
2AL	2.55	0.574	0.581	1.2
3AL	2.92	0.592	0.597	0.9
5AL	2.99	0.475	0.461	3.2
8AL	3.30	0.482	0.486	0.6
9AL	3.16	0.480	0.493	2.7
4AL	2.67	0.505	0.503	0.4
6AL	3.02	0.436	0.434	0.5

A simplified procedure, that allows us to evaluate the emissivity value using the $w_{mz,i}(e_{LB})$ value obtained from the parameter map as input for the emissivity map, was obtained. (Figure 18). We can recap it as follows:

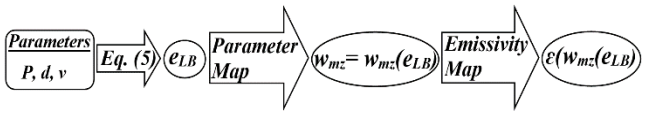

Figure 18. Simplified procedure.

- *Known the working parameters, through the Eq. (5) the value of specific energy e_{LB} is calculated.*
- *Using the parameter map, the value $w_{mz} = w_{mz,i}(e_{LB})$ was obtained.*
- *Using the emissivity map, the value $\varepsilon(w_{mz}(e_{LB}))$ was obtained.*

The simplified procedure was faster and leaner than the standard one. In fact, the simplified procedure foresees to use as input for the emissivity map the value $w_{mz,i}(e_{LB})$ obtained through Eq. (5) and parameter map. This process is much simpler and faster than using the FEM model.

5. Conclusion

To use an infrared camera to measure the temperature during laser welding, it is necessary to know the emissivity. For this type of processing, the emissivity value is obtained by comparing the width of the melted zone with the temperature distribution measured in the laser irradiation zone. The apparent temperature value corresponding to the width of the molten zone is obtained. Finally, using Planck's law, the emissivity value may be calculated.

Since the emissivity is not constant, every time the working parameters are set, it will be necessary to carry out a preliminary test. This results in a waste of time and materials. The methodology is not very workable and laborious to use. In this work, two procedures, that can overcome the limits seen, have been proposed. Both procedures (Standard – Simplified) require the use of the emissivity map. The knowledge of the emissivity map allowed a relationship between the width of the melted zone

and the emissivity, corresponding to a preselected value for the defocus. This allowed it to value the emissivity after setting parameters and measuring the width of the melted zone ($w_{mz} = \rho_y$) by FEM model (Standard procedure). The time needed to obtain the emissivity value corresponds to the time needed to obtain the value ρ_y using the FEM model (about 4 hours). To reduce the time required, and thereby obtain a more practical procedure, a parameter map was calculated. The knowledge of the parameter map allowed a relationship between specific energy and the width of the melted zone, corresponding to a preselected value for the defocus. It was able to value the width of the melted zone $w_{mz} = w_{mz,i}(e_{LB})$ after fixed parameters and calculated the specific energy. The $\varepsilon(w_{mz,i}(e_{LB}))$ value is obtained through the emissivity map. In this way, a more streamlined and rapid procedure was obtained (Simplified procedure), for which calculation times are, de facto, zero. In this way, after setting the working parameters, it is possible to get an instant evaluation of the emissivity without having to perform preliminary tests. Both methods are quick and allow us to determine the emissivity value considering the physical phenomena involved and the conditions of the surface.

Nomenclature

def	Focal beam waist	mm
r_0	Radius beam	mm
v	Welding speed	mm s^{-1}
w_{mz}	Width of the melted zone	mm
ρ_y	Isotherm corresponding to the melting point	mm
P	Power	W
L_x	Slab length	mm
L_y	Slab width	mm
L_z	Slab depth	mm
C_{abs}	Absorption coefficient	/
k	Thermal conductivity	$Wm^{-1}K^{-1}$
h	Convective heat transfer coefficient	$Wm^{-2}K^{-1}$
ε_{irr}	Aluminum emissivity constant value for a FEM model	/
ρ	Mass density	Kg m^{-3}
c_p	Specific heat.	J kg^{-1} K^{-1}
μ	Dynamic Viscosity	Pa s
σ	Surface tension coefficient	N m^{-1}
L_m	Latent heat of fusion	J kg^{-1}
L_v	Latent heat of vaporization	J kg^{-1}
T_m	Melting temperature	K
T_{vap}	Evaporation temperature	K
M	Molar mass	kg mol^{-1}
R	Ideal gas constant	J·mol^{-1} K^{-1}

References:

[1] A. Mosavia, F. Salehib, L. Nadaie, S. Karolyc, N. E. Gorjid, "Modeling the temperature distribution during laser hardening process", *Results in Physics Volume 16*, March 2020, 102883. https://doi.org/10.1016/j.rinp.2019.102883.

[2] H.G. Woo, H. S. Cho, "Three-dimensional temperature distribution in laser surface hardening processes", *Proceedings of the Institution of Mechanical Engineers Part B Journal of Engineering Manufacture* 213(7):695-712. DOI:10.1243/0954405991517128.

[3] I. Smurv and M. Doubenskaia, "Temperature Monitoring by Optical Methods in Laser Processing", *Chapter 9 in the Book ''Laser-Assisted Fabrication of Materials''. Springer Series in Materials Science, Vol 161*, J. Dutta Majumdar and I. Manna, Ed., Springer, Berlin, 2013, p 373-422. DOI:10.1007/978-3-642-28359-8_9.

[4] M. Doubenskaia, M. Pavlov, S. Grigoriev, I. Smurov, "Definition of brightness temperature and restoration of true temperature in laser cladding using infrared camera", April 2013, *Surface and Coatings Technology 220:244-247.* DOI: 10.1016/j.surfcoat.2012.10.044.

[5] M. Doubenskaia, I. Zhirnov, V. Teleshevskiy, Ph. Bertrand, I. Smurov, "Determination of True Temperature in Selective Laser Melting of Metal Powder Using Infrared Camera" November 2015 *Materials Science Forum 834:93-102.* DOI:10.4028/ www.scientific.net/MSF.834.93.

[6] Z. Lanc, B. Strbac, M. Zeljkovic, A Zivkovic, M Hadzistevic, "Emissivity of aluminium alloy using infrared thermography technique", June 2018, *Materials and Technologies 52(3).* DOI:10.17222/mit.2017.152.

[7] A. P Tadamalle, "Review of Real-Time Temperature Measurement for Process Monitoring of Laser Conduction Welding", *Eng. Sci. Technol. An Int. J. 2(5), 946–950 (2012).*

[8] S. M. Thompson, L. Bian, N. Shamsaei, A. Yadollahi, "An overview of Direct Laser Deposition for additive manufacturing, Part I: Transport phenomena, modeling and diagnostics", *Addit. Manuf. 8, 36–62, Elsevier B.V. (2015).* https://doi.org/10.1016/j.addma.2015.07.001.

[9] T. Staudt, E. Eschner, M. Schmidt, "Temperature determination in laser welding based upon a hyperspectral imaging technique", *CIRP Annals Volume 68, Issue 1, 2019, Pages 225-228.* https://doi.org/10.1016/j.cirp.2019.04.117.

[10] M. Miccio, R. Pierri, G. Cuccurullo, A. Metallo, P. Brachi, "Process intensification of tomato residues drying by microwave heating: experiments and simulation", *August 2020 Chemical Engineering and Processing 156:108082. DOI: 10.1016/j.cep.2020.108082.*

[11] I. Mudawar, "Emissivity characteristics of roughened aluminum alloy surfaces and assessment of multispectral radiation thermometry (MRT) emissivity models", *International Journal of Heat and Mass Transfer · August 2004.* DOI: 10.1016/j.ijheatmasstransfer.2004.04.025.

[12] I. Mudawar, "Experimental Investigation of Emissivity of Aluminum Alloys and Temperature Determination Using Multispectral Radiation Thermometry (MRT) Algorithms", *Journal of Materials Engineering and Performance · January 2002*. DOI: 10.1361/105994902770343818.

[13] Z. Lanc, B. Strbac, M. Zeljkovic, A. Zivkovic, M. Hadzistevic, "Emissivity of aluminium alloy using infrared thermography technique", *June 2018 Materials and Technologies.* doi:10.17222/mit.2017.152.

[14] C. Bonacina, G. Comini, A. Fassano, M. Primicerio, "Numerical solutions of phase change problems", *International Journal of Heat Mass Transfer, 16, 1825-1832 (1973)]*.

[15] C. J. Knight, "Theoretical modeling of rapid surface vaporization with back pressure", *American Institute of Aeronautics and Astronautics Journal, 17:5, 19–523 (1979).*

[16] M. Edstorp, "Weld Pool Simulations", in *Department of Mathematical Sciences (2008), Chalmers University of Technology and University of Gothenburg*. ISSN 1652-9715

[17] R. Fabbro, K. Chouf," "Dynamical description of the keyhole in deep penetration laser welding*", Journal of Laser Applications,12:4,142-148- (2000).* https://doi.org/10.2351/1.521924.

[18] K. Narender, A. Sowbhagya M. Rao, K. Gopal K. Rao, N. Gopi Krishna, "Temperature Dependence of Density and Thermal Expansion of Wrought Aluminum Alloys 7041, 7075 and 7095 by Gamma Ray Attenuation Method", *Journal of Modern Physics 4(03):331-336; January 2013* DOI:10.4236/jmp.2013.43045.

[19] M. Leitner, T. Leitner, A. Schmon, K. Aziz, G. Pottlacher, "Thermophysical Properties of Liquid Aluminum *(2017)", Metallurgical and Materials Transactions A volume 48, pages3036–304.* DOI: 10.1007/s11661-017-4053-6

[20] R. Paschotta, Encyclopedia of Laser Physics and Technology, "*Wiley-VCH: Berlin, Germany, Vch Pub; 2° edition (22 October 2008)".* ISBN-10: 9783527408283.

[21] K. Suresh Kumar, T. Sparks, F. Liou, "Parameter determination and experimental validation of a wire feed Additive Manufacturing model", *In Proceedings of the 29th Annual International Solid Freeform Fabrication Symposium; An Additive Manufacturing Conference, Austin, TX,USA,pg.13–15;August-2015;URI.* https://hdl.handle.net/2152/89407.

[22] I. Bunaziv, Odd M. Akselsen, X. Ren, B. Nyhus and M. Eriksson, "Laser Beam and Laser-Arc Hybrid Welding of Aluminium Alloys", *Metals 2021, 11(8), 1150.* https://doi.org/10.3390/met11081150.

[23] J. Heigel, P. Michaleris, E. Reutzel, "Thermo-mechanical model development and validation of directed energy deposition additive manufacturing of Ti-6Al-4V", *Additive Manufacturing Volume 5, January 2015. Pages 9-19.* https://doi.org/10.1016/j.addma.2014.10.003.

[24] I. Smurov, M. Doubenskaia, "Laser-Assisted Fabrication of Materials", *in Majumdar J. D. and Manna I. (eds.), (Springer Series in Materials Science 161, Springer-Verlag Berlin Heidelberg, 2013, pp. 373-422.)* DOI:10.1007/978-3-642-28359-8.

[25] E. Filep, D. N. Kutasi, L. Kenéz, "Method for Emissivity Estimation of Metals*", Acta Materialia Transylvanica, 1/1, 2018 pg. 31-36.* https://doi.org/10.2478/amt-2018-0010.